Geophysical Journal International

Geophys. J. Int. (2019) **219,** 607–618
Advance Access publication 2019 July 11
GJI Seismology

doi: 10.1093/gji/ggz314

Upper-mantle shear velocity structure beneath the equatorial East Pacific Rise from array-based teleseismic surface wave dispersion analysis

Qiushi Zhai,[1,2] Huajian Yao[1,3] and Zhigang Peng[2]

[1] *Laboratory of Seismology and Physics of Earth's Interior, School of Earth and Space Sciences, University of Science and Technology of China, Hefei 230026, China. E-mail:* *hjyao@ustc.edu.cn*
[2] *School of Earth and Atmospheric Sciences, Georgia Institute of Technology, Atlanta, GA 30332, USA*
[3] *National Geophysical Observatory at Mengcheng, University of Science and Technology of China, Anhui 233500, China*

Accepted 2019 July 10. Received 2019 June 26; in original form 2018 July 19

SUMMARY

The Discovery/Gofar transform fault system is associated with a fast-spreading centre on the equatorial East Pacific Rise. Most of the previous studies focus on its regular seismic cycle and crustal fault zone structure, but the characteristics of the upper-mantle structure beneath this mid-ocean ridge system are not well known. Here we invert upper-mantle shear velocity structure in this region using both teleseismic surface waves and ambient seismic noise from 24 ocean bottom seismometers (OBSs) deployed in this region in 2008. We develop an array analysis method with multidimensional stacking and tracing to determine the average fundamental mode Rayleigh-wave phase-velocity dispersion curve (period band 20–100 s) for 94 teleseismic events distributed along the E-W array direction. Then, we combine with the previously measured Rayleigh-wave phase-velocity dispersion (period band 2–25 s) from ambient seismic noise to obtain the average fundamental mode (period band 2–100 s) and the first higher mode (period band 3–7 s) Rayleigh-wave phase-velocity dispersion. The average dispersion data are inverted for the 1-D average shear wave velocity (Vs) structure from crust to 200-km depth in the upper mantle beneath our study region. The average Vs between the Moho and the 200-km depth of the final model is about 4.18 km s^{-1}. There exists an ∼5-km thickness high-velocity lid (LID) beneath the Moho with the maximum Vs of 4.37 km s^{-1}. Below the LID, the Vs of a pronounced low-velocity zone (LVZ) in the uppermost mantle (15–60-km depth) is 4.03–4.23 km s^{-1} (∼10 per cent lower than the global average). This pronounced LVZ is thinner and shallower than the LVZs beneath other oceanic areas with older lithospheric ages. We infer that partial melting (0.5–5 per cent) mainly occurs in the shallow upper-mantle zone beneath this young (0–2 Myr) oceanic region. In the deeper portion (60–200-km depth), the Vs of a weak LVZ is 4.15–4.27 km s^{-1} (∼5 per cent lower than the global average). Furthermore, the inferred lithosphere–asthenosphere boundary with ∼15-km thickness can fit well with the conductive cooling model. These results are useful for understanding the depth distribution and melting characteristics of the upper-mantle lithosphere and asthenosphere in this active ridge-transform fault region.

Key words: Composition and structure of the mantle; Pacific Ocean; Time-series analysis; Surface waves and free oscillations; Mid-ocean ridge processes.

1 INTRODUCTION

New oceanic lithospheres are generated at mid-ocean ridges (MORs) such as the East Pacific Rise (EPR) along the floor of the Pacific Ocean. Direct measurement of seismic velocity structures beneath oceanic spreading centres is essential for understanding the dynamic system of MORs as well as the distribution and migration of melted magma beneath the MORs. In addition, such a measurement could be used to test conductive cooling models (Harmon *et al.* 2009). Recent seismic tomographic studies based on ambient noise as well as regional and teleseismic earthquake data recorded by ocean bottom seismometers (OBSs) greatly improved our understanding of seismic structures beneath the EPR (Forsyth *et al.* 1998, 2006; Webb & Forsyth 1998; Evans *et al.* 2005; Gu 2005;

© The Author(s) 2019. Published by Oxford University Press on behalf of The Royal Astronomical Society.

Harmon *et al.* 2007, 2009; Weeraratne *et al.* 2007; Yao *et al.* 2011). These studies generally found a seismic low-velocity zone (LVZ) beneath a high-velocity lid (LID) in the uppermost mantle beneath the EPR region. However, the obtained seismic velocities and the depth extents of the LID and LVZ are widely distributed, suggesting that the distribution and migration of melt, its thermal structure and mantle flow pattern may be different among the different segments of the EPR (Dunn & Forsyth 2003).

The characteristics of fault structure and seismic cycle (moment magnitude M_w ~6.0 earthquakes occur every ~5 yr) in the Discovery/Gofar (DG) transform fault system on the equatorial EPR (Fig. 1) are the subjects of several recent studies (McGuire *et al.* 2005, 2012; McGuire 2008; Pickle *et al.* 2009; Roland *et al.* 2012; Froment *et al.* 2014; Géli *et al.* 2014; Wolfson-Schwehr *et al.* 2014). Furthermore, the average crust and the uppermost mantle structure in this region have been well resolved by the dispersion curve of the fundamental-mode (period band 2–30 s) and the first-higher-mode (period band 3–7 s) Rayleigh waves from ambient seismic noise recorded by the OBSs (Yao *et al.* 2011). However, due to the limited depth penetration, the mantle structure beneath cannot be well constrained by using ambient seismic noise alone.

A combination of long-period teleseismic surface waves and short- to intermediate-period ambient noise data has enabled seismic imaging of both the crust and the upper-mantle structure in the oceanic regions, for example, the EPR in the south-central Pacific (Harmon *et al.* 2007), the central Pacific Ocean (the NoMelt Experiment; Lin *et al.* 2016), the northwestern Pacific Ocean (Takeo *et al.* 2013, 2018), the southeastwards of Tahiti island in the South Pacific (Takeo *et al.* 2016), the Tonga-Lau-Fiji region (Wei *et al.* 2016) and the offshore region of New Zealand's South Island (Ball *et al.* 2016). Motivated by these studies, here we plan to obtain a more accurate 1-D upper-mantle (above 200 km depth) Vs model beneath the DG transform fault system (latitude: 3.8°–4.8°S, longitude: 106.5°–104°W) on the equatorial EPR (Fig. 1). We first develop an array analysis method for teleseismic surface wave dispersion measurements and apply it to the vertical-component broadband data recorded by 24 OBSs deployed in this study region. Next, we measure the average phase-velocity dispersion (period band 20–100 s) of the fundamental-mode Rayleigh wave from teleseismic events. Then we combine it with the previously measured dispersion data (period band 2–25 s) from ambient seismic noise (Yao *et al.* 2011) to invert for the 1-D average Vs structure model of the crust and the upper mantle beneath this region. Moreover, we describe the main characteristics of the LID and the LVZ in this region and discuss the thickness of oceanic lithosphere with a conductive cooling model (Harmon *et al.* 2009).

2 DATA

Based on a regular seismic cycle for M~6 events on the EPR (McGuire *et al.* 2005, 2012), a temporary OBS seismic experiment was conducted at the Quebrada/Discovery/Gofar (Q/D/G) transform fault system on the equatorial EPR in 2008 (McGuire 2008; Yao *et al.* 2011; Froment *et al.* 2014; Wolfson-Schwehr *et al.* 2014). The OBS array was deployed for about 1 yr. The vertical-component data of 24 broad-band sensors (Guralp CMG-3T seismometers) in this OBS array are used for the surface wave phase-velocity dispersion analysis presented in this study (Fig. 1). Among these sensors, 8 OBSs are around the Discovery fault and 16 OBSs are around the Gofar fault.

3 ARRAY-BASED TELESEISMIC SURFACE WAVE DISPERSION ANALYSIS

In this section, we introduce an array-based multidimensional imaging analysis method to measure average phase-velocity dispersions of the fundamental-mode Rayleigh waves. The analysed data are generated by 94 teleseismic events with moment magnitudes M_w between 5.7–7.3, depths shallower than 100 km and great-circle distances between 20° and 150° (Fig. 2). These events are located within ±20° along the direction from the Discovery OBS array to the Gofar OBS array (Figs 1 and 2). We measure the average phase-velocity dispersion for these teleseismic events by a four-step array-based multidimensional imaging analysis approach: (1) pre-processing, (2) frequency-domain phase shifting and time-domain waveform stacking, (3) phase-velocity dispersion curve tracing and (4) dispersion averaging. Then we combine the average dispersion from teleseismic events with the average dispersion from ambient noise to obtain the broad-band average phase-velocity dispersion curve.

3.1 Pre-processing

We apply typical pre-processing steps on the original seismic waveforms of these 94 teleseismic events. First, we remove the instrument responses, means and trends from all vertical-component seismic waveforms. Second, we cut the surface wave records for each station and each event with a group-velocity window (2–5 km s^{-1}). Next, we apply a bandpass (period band 10–160 s) filter on these surface waveforms and then normalize them. We also manually delete bad traces. Finally, we obtain the normalized teleseismic surface waveforms for the next step. Fig. 3 shows the surface waveforms of an example teleseismic event occurred in the Kermadec-Tonga subduction zone.

3.2 Frequency-domain phase shifting and time-domain waveform stacking

We develop an array-based multidimensional imaging analysis method for teleseismic surface waves to measure the phase-velocity dispersion by frequency-domain phase shifting and time-domain waveform stacking. When a small-scale array records teleseismic surface waves, a time-harmonic wavefield at the angular frequency ω could be represented as follows:

$$\tilde{\psi}\ (r, t, \omega) = \mathcal{A}(\omega) \exp\left(i\varphi\left(r, t, \omega\right)\right) \tag{1a}$$

$$\varphi\ (r, t, \omega) =\ kr - \omega t + \varphi_0(\omega) \tag{1b}$$

where $\tilde{\psi}(r, t, \omega)$ is the wave field, r is the distance of the great-circle path, t is the propagation time, $\mathcal{A}(\omega)$ is the amplitude at the angular frequency ω, $\varphi(r,\ t,\ \omega)$ is the phase, k is the wavenumber and $\varphi_0(\omega)$ is the initial phase of the earthquake. We assume that surface waves propagate along the great-circle paths, which are nearly identical before arriving at the array. The difference of $\mathcal{A}$ at different distance r can be ignored due to the previous normalization. Therefore, the difference of $\tilde{\psi}(r, t, \omega)$ at different r can be simply attributed to the difference of $\varphi(r, t, \omega)$. For example, A is the nearest (minimum great-circle path) station in the seismic array for a given teleseismic event E, and B is another station in this array (Fig. 4). So the phase

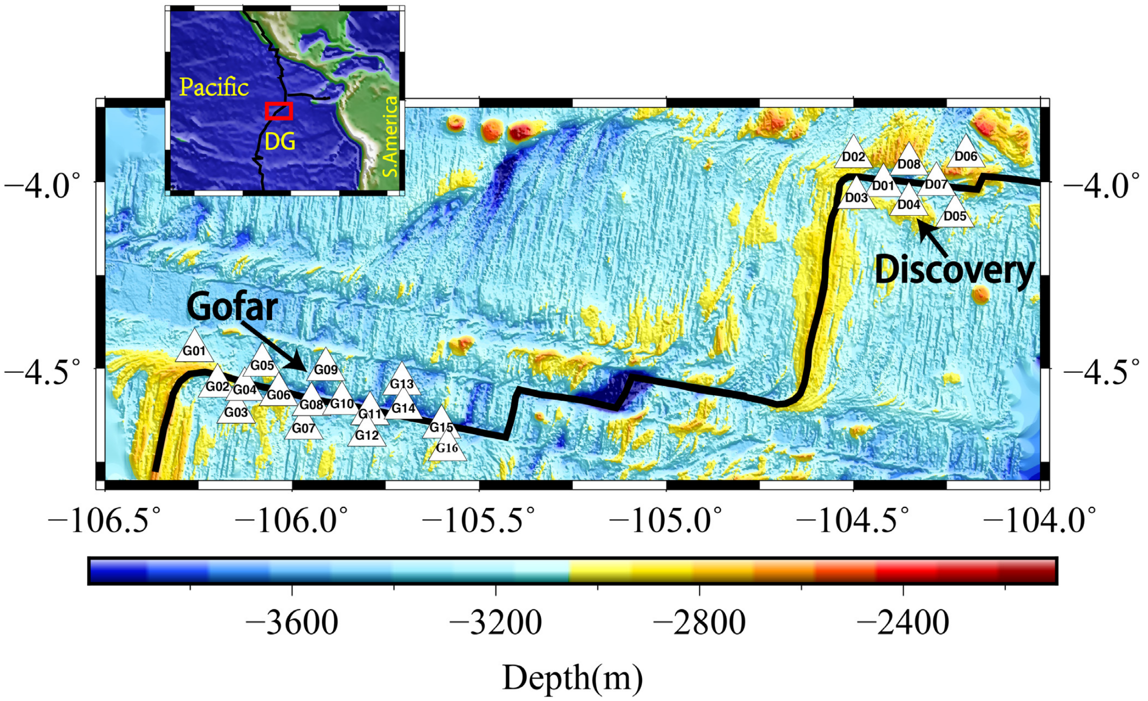

Figure 1. Bathymetry (Langmuir & Forsyth 2007; Pickle *et al.* 2009) and locations of the 24 broad-band ocean bottom seismometers (OBSs) (white triangles) around the Discovery/Gofar (DG) transform fault region on the Eastern Pacific Rise (EPR) south of the equator. The black lines mark the middle ocean ridges and transform faults (Beaulieu *et al.* 2019). The inset marks the study region in a larger map of the Pacific Ocean and Latin America.

difference between stations A and B could be written as follows:

$$\begin{aligned}\Delta\varphi_{\mathrm{AB}}\ (\omega, c(\omega)) &= \varphi_{\mathrm{B}} - \varphi_{\mathrm{A}} = k_{\mathrm{B}}\, r_{\mathrm{B}} - k_{\mathrm{A}} r_{\mathrm{A}} \\ &\approx [k_{\mathrm{A}} r_{\mathrm{A}} + k_{\mathrm{AB}}\,(r_{\mathrm{B}} - r_{\mathrm{A}})] - k_{\mathrm{A}}\, r_{\mathrm{A}} \\ &= \frac{\omega}{c\,(\omega)}\ (r_{\mathrm{B}} - r_{\mathrm{A}})\end{aligned} \tag{2}$$

where $\Delta\varphi_{\mathrm{AB}}$ is the phase difference, $k_{\mathrm{AB}} = \frac{\omega}{c(\omega)}$ is the average wave number between A and B in this array, and $c(\omega)$ is the average phase velocity at the angular frequency ω of the array region.

Based on the phase difference shown in the eq. (2), we apply frequency-domain phase shifting to the pre-processed waveforms at all stations in the DG array for a given teleseismic event E as eq. (3):

$$U_i^s\,(\omega, c\,(\omega)) \ = U_i\ \ (\omega) \exp\left(-i\,\Delta\varphi_i\,(\omega, c\,(\omega))\right) \tag{3a}$$

$$\Delta\varphi_i\ (\omega, c\,(\omega)) = \varphi_i\ -\ \varphi_{i_0} = \frac{\omega}{c\,(\omega)}\ \left(r_i - r_{i_0}\right) \tag{3b}$$

$$U_i\,(\omega) = \mathcal{F}\,(u_i\,(t)) \tag{3c}$$

where i is the station index, U_i^s is the frequency spectrum after phase shifting of the ith station records, U_i is the original frequency spectrum, $\Delta\varphi_i$ is the phase difference between the ith station and the nearest station i_0 for the event E, $\mathcal{F}$ is the Fourier Transform and $u_i(t)$ is the pre-processed waveforms of the ith station in the time domain. In order to make reliable measurements at long periods, we require $r_i - r_{i_0}$ to be at least half the wavelength (Yao *et al.* 2006). After applying this to each station in the array, we shift the waveforms of all stations to align with the waveform of the i_0 station. Next, we stack all shifted waveforms in the time domain as

$$P\,(\omega,\ c\,(\omega)\,, t) = \mathrm{Env}\left[\sum\nolimits_i \alpha_i \mathcal{F}^{-1}\left(U_i^s\,(\omega, c\,(\omega))\,G\,(\omega)\right)\right] \tag{4}$$

where P is the 3-D (ω, $c(\omega)$ and t) amplitude matrix after stacking, 'Env' operator means taking the envelope of the trace (Fig. 5b), α_i is the weight of ith station that is equal to the inverse of the number of stations in the D subarray or G subarray to make sure that the two subarrays have the same weights in total (Fig. 1). $\mathcal{F}^{-1}$ is the inverse Fourier Transform, and $G(\omega)$ is the Gaussian window in the frequency domain as a narrow bandpass filter. The reason why we need to stack in the time domain instead of the frequency domain is that we could easily separate wavepackets of different phases with different group velocities in the time domain. In this way, we can better estimate phase velocities $c(T)$ of the fundamental-mode surface waves.

The relationship between the period T and angular frequency ω, as well as the relationship between the average group velocity g from the source of the event E to the i_0 nearest station and the great-circle distance r of nearest station i_0, can be written as

$$T \ = \ 2\pi/\omega, \tag{5a}$$

$$g \ = \ r_{i_0}\ /t. \tag{5b}$$

As shown in eq. (5), we can transfer the 3-D amplitude matrix P from the ω, $c(\omega)$ and t domains to the T, $c(T)$ and $g(T)$ domains as

$$P\ (T,\ c\,(T)\,, g\,(T)) = \ P\,(\omega,\ c\,(\omega)\,, t)\,. \tag{6}$$

In this study, we set the period T range as 20–100 s with a 2.5 s interval. We set the phase velocity $c(T)$ range as 2–5 km s^{-1} with a 0.01 km s^{-1} interval. In addition, we set the group velocity $g(T)$ range as 2.5–4.5 km s^{-1}, but we do not use linear intervals. We use 1 s as the linear interval for the time t. Based on eq. (5b), we obtain the range of the interval $g(T)$, 0.002–0.003 km s^{-1}.

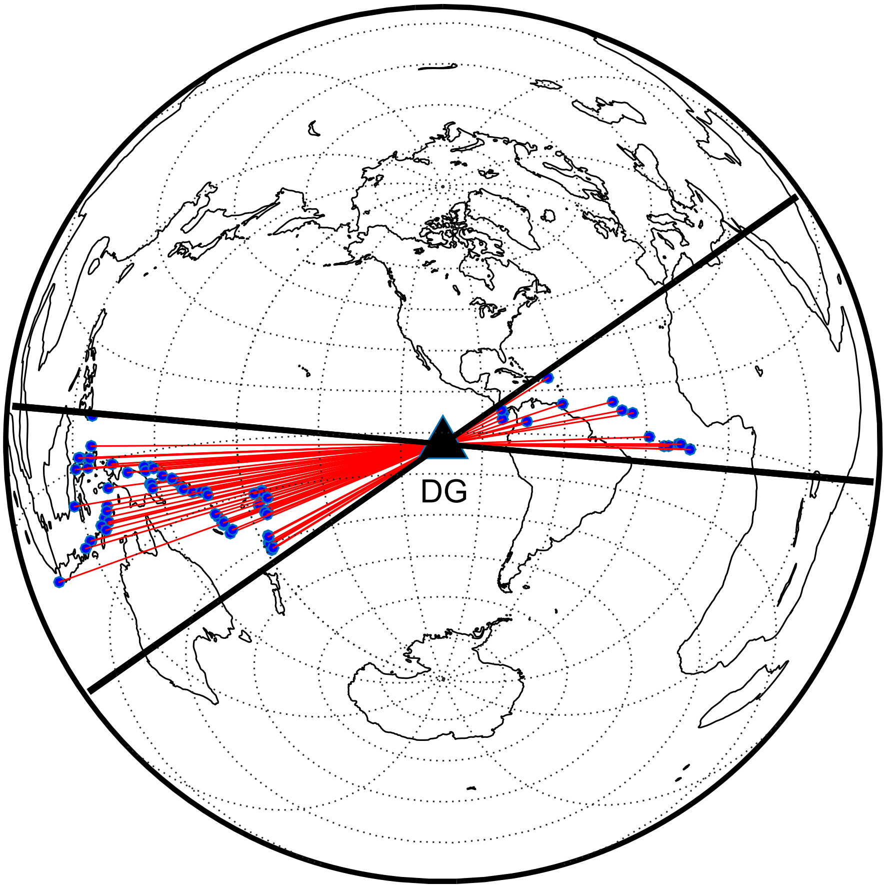

Figure 2. Locations of 94 teleseismic events (blue dots) and the DG transform fault region (black triangle). The red lines are the great-circle paths from earthquakes (blue dots) to the DG region. The bold black lines indicate the ±20° off the direction from the Discovery OBS array to the Gofar OBS array (Fig. 1).

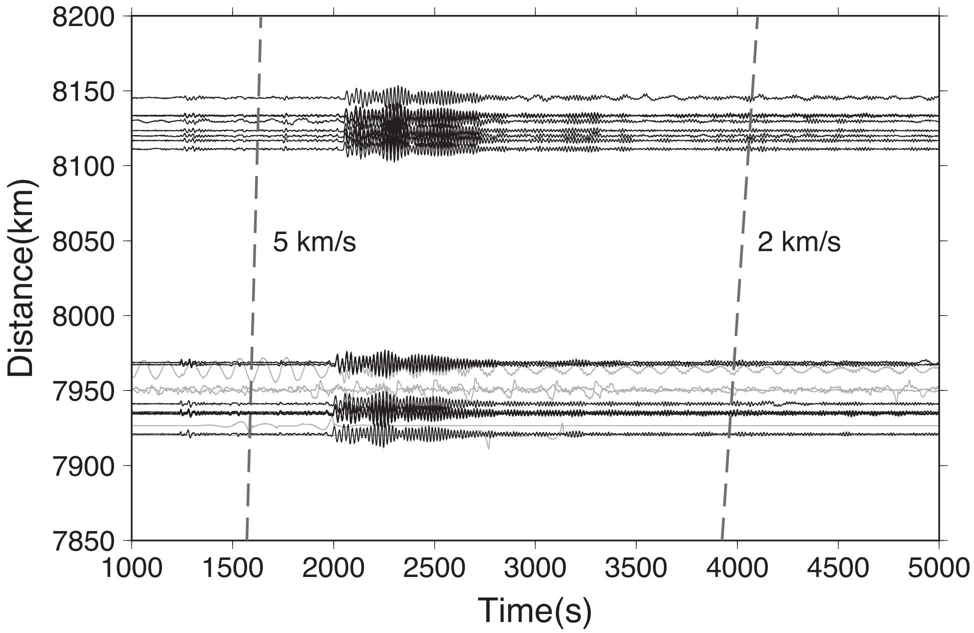

Figure 3. Vertical-component surface waveforms after pre-processing of one teleseismic event recorded by the DG OBS array (Fig. 2). The event parameter is listed on the top (2008/12/09 06:23:59, M_{w}: 6.7, latitude: −31.23°, longitude: –176.92° and depth: 18 km). The distance is the length of the great-circle path, and the waveforms are aligned by the origin time of this earthquake. The two dashed lines mark the reference group velocities of 5 and 2 km s^{-1}. The grey lines are manually deleted bad traces.

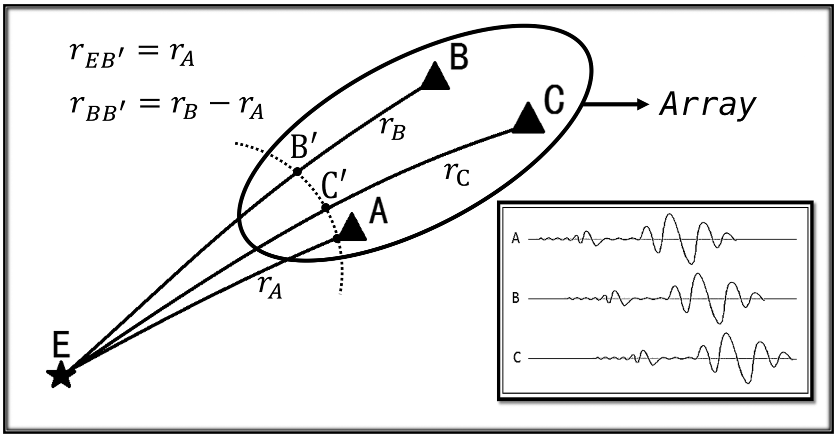

Figure 4. A schematic showing the array analysis method of teleseismic surface wave dispersion (eqs 1–6). The great-circle paths (black curves) connect the teleseismic event (black star) to the stations (black triangles).

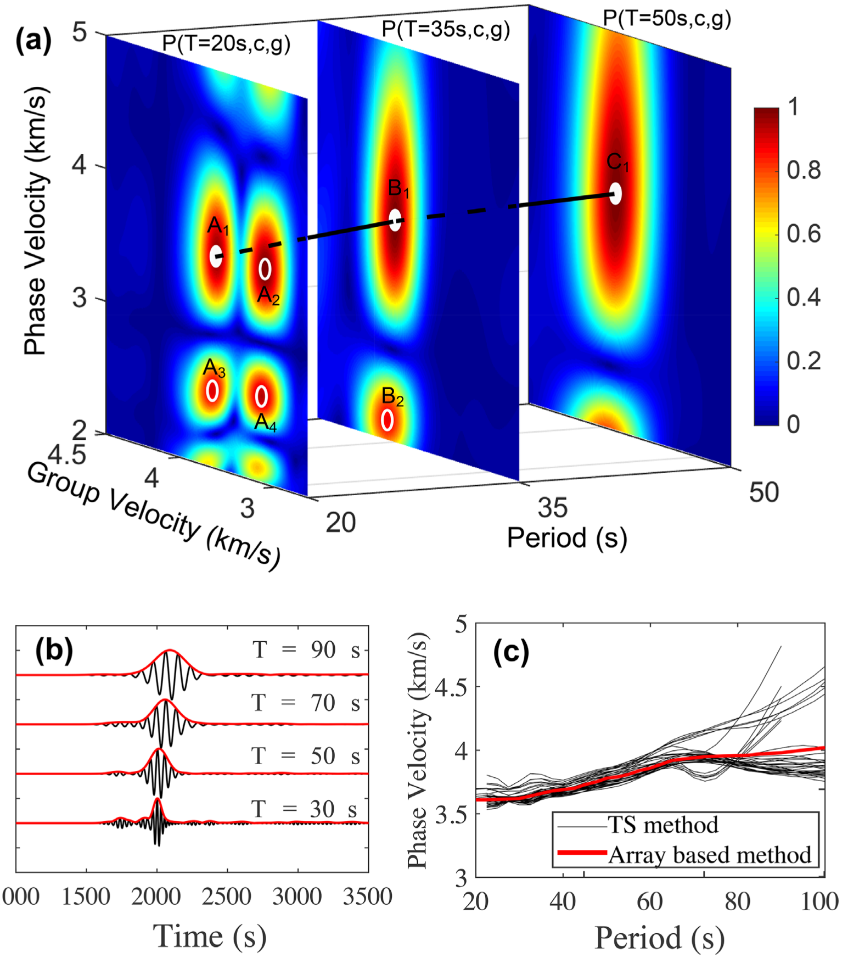

Figure 5. (a) The 3-D amplitude matrix (eq. 6) for phase-velocity dispersion curve tracing of an example event (Fig. 3). We present three example slices of this 3-D amplitude matrix at periods of 20, 35 and 50 s. Solid and open circles are the local maxima of each slice, and the solid circles (A_1, B_1 and C_1) are the final selected local maximum of each period, respectively. The black line represents a sketch of the final phase-velocity dispersion curve. (b) The shifted-stacked traces (black lines) and their final envelope (red lines) for a few narrow-band frequencies of the same event in panel (a). (c) The comparison of our array-based method and the TS method applying to the same event in panel (a). The black lines are the dispersion curves measured from different station pairs. The red line is the dispersion curve measured from the entire array with our array-based method.

3.3 Phase-velocity dispersion curve tracing

For each teleseismic event, we obtain a 3-D amplitude matrix (eq. 6) after the frequency-domain phase shifting and time-domain waveform stacking. Next, we need to trace a reasonable phase-velocity dispersion curve from a 3-D amplitude matrix (Fig. 5a). In an ideal case, we just need to find out the velocity value corresponding to the global maximum of the 2-D matrix at each period of the 3-D matrix, and then put them together to obtain a complete phase-velocity dispersion curve. In reality, we may have multiple local maxima corresponding to different phases or modes (Fig. 5a). In such cases, some local maxima may be more reasonable for the fundamental mode dispersion according to some physical constraints, such as the range and continuity of the fundamental Rayleigh-wave phase velocity and group velocities. In this study, we set up a reasonable range of regional phase velocity as 2–5 km s^{-1} and a reasonable range of teleseismic group velocity as 2.5–4.5 km s^{-1} for the period band of 20–100s.

To trace the dispersion curve, we first retain the largest four or less local maxima for each period, such as A$_i$ for $T = 20$ s, B$_i$ for $T = 35$ s, and C$_i$ for $T = 50$ s, as shown in Fig. 5(a). Then we set up one reasonable local or global maximum as the 'initial tracing point' of the dispersion tracing, such as C$_1$ for $T = 50$ s in Fig. 5(a). To trace the best local maxima for a given period T_i from the start point of the selected reference period T_{i_0}, we need to calculate the 'velocity distance' of the local maxima of T_i as

$$l_{ij} = \sqrt{\left(c_{ij} - c_{i_0 j_0}\right)^2 + \left(g_{ij} - g_{i_0 j_0}\right)^2} \tag{7}$$

where i is the index of a nearby period with respect to the selected reference period with the index i_0, that is, $i = i_0 + 1$ or $i = i_0 - 1$, j is the index of local maxima ($j = 1, 2, 3$ or 4), j_0 is the index of the local maxima of the selected reference period T_{i_0}, and l_{ij} is the velocity distance of the jth local maxima of period T_i. Then the local maxima of nearby periods with the minimum velocity distance are selected as the 'tracing point' for the next step dispersion point tracing. Repeating this procedure, we then obtain a dispersion curve $c_{i_0 j_0}(T)$ from these 'tracing points'.

To start this process, we need an initial tracing point of an initial period. After analysing the stability of all results of the DG data set, we decide to set up the global maximum at $T = 60$ s as the initial tracing point and then trace the dispersion towards 20 and 100 s. After tracing the phase-velocity dispersion curves of all events, we manually remove some unreasonable parts of dispersion curves based on the value and slope range of the dispersion (see Supporting Information Fig. S1). The final selected dispersion curves of different teleseismic events are shown as grey lines in Fig. 6.

3.4 Dispersion averaging

Next, we calculate the average fundamental mode Rayleigh-wave phase-velocity dispersion for the DG region (Fig. 6). We use the standard deviation of the mean (Lin & Ritzwoller 2011) to estimate the measurement error. The overall trend of the average phase-velocities at periods of 20–100 s approximately increases linearly from ∼3.7 to ∼4.0 km s^{-1}. The measurement error (less than 1.5 per cent) also increases with the period, due to the decrease of numbers of the qualified teleseismic events at longer periods (Fig. 6). At shorter periods (fundamental mode: 2–25 s, first-higher mode: 3–7 s), we use the average phase-velocity dispersion from ambient noise analysis of the same data recorded by the DG array in 2008 (Yao *et al.* 2011). In the overlapping period range (20–25 s), the average velocities from teleseismic events and ambient noise are slightly different (∼1.5 per cent on average). We simply average and smooth the overlapping measurements (Figs 6 and 7a). Finally, we obtain the average broad-band phase-velocity dispersion data of the fundamental mode and the first-higher mode (Figs 6 and 7a) Rayleigh waves, which are then used for inversion of the average crustal and upper-mantle Vs structure beneath the DG region (Fig. 7b).

3.5 Compared with the two-station analysis method

A two-station (TS) analysis method based on narrow-banding filtering and cross-correlation is normally used to measure interstation phase-velocity dispersion (i.e. Yao *et al.* 2006; Lin *et al.* 2016). Such TS method could measure a dispersion curve for each station pair, resulting in many curves for multiple stations (black lines in Fig. 5c). In comparison, our array-based method could measure an average dispersion curve for multiple stations of an array (red line in Fig. 5c). Fig. 5(c) shows an example of high-quality data generated by the same event in Fig. 3. While the results of these two methods match well with each other, the result of our array-based method is more stable and smooth at long and short periods (e.g. $T = 20$ s in Fig. 5a).

4 INVERSION OF 1-D UPPER-MANTLE STRUCTURE

The phase velocity of the fundamental-mode Rayleigh wave at intermediate and longer periods is less sensitive to the compressional velocity and the density of the medium, but more sensitive to the shear velocity at a depth of around 1/3 of its wavelength (Fig. 8). Based on such characteristics, we can resolve the shear velocity structure approximately above 200-km depth (especially between the Moho and 150-km depth) from our phase-velocity data. An iterative, weighted inversion method based on damped least squares (Herrmann 2013) is used to invert for the shear velocity structure from these dispersion data. The variance of phase-velocity data is based on the measurement error instead of residual in the inversion. The water layer and crust structure of the initial model above the Moho are from Yao *et al.* (2011), and the upper-mantle structure of the initial model beneath the Moho is from the ak135-F spherical average model (Kennett *et al.* 1995; Montagner & Kennett 1996). The initial model between the Moho and 100-km depth is divided into 5-km-thick layers, and the initial model between the 100-km and 200-km depth is divided into 10-km-thick layers. During the inversion, we apply a constraint in velocity changes between immediately adjacent layers and fix the damping value as 2 in order to obtain a smooth 1-D model (see Section 3 and Supporting Information Table S2). In the meantime, we fix the Vp/Vs ratio as 1.80 for the crustal structure (Yao *et al.* 2011), as well as 1.88 for the upper-mantle structure (Harmon *et al.* 2007). The density is computed from the Vp using the empirical relationship given by Brocher (2005).

The final model obtained after the inversion is shown in Figs 7(b) and 9, as well as listed in Table 1. The observed phase-velocity dispersion curves and the predicted dispersion from the final inversion result are shown in Fig. 7(a). To estimate the error of the inversion result, we generate a series of Gaussian random noise with its standard deviation setting as the measurement error of the average dispersion at the corresponding period (Fig. 7a). We add random noise to the observed average phase-velocity data. Then we investigate the bias of the obtained model caused by adding noise in the

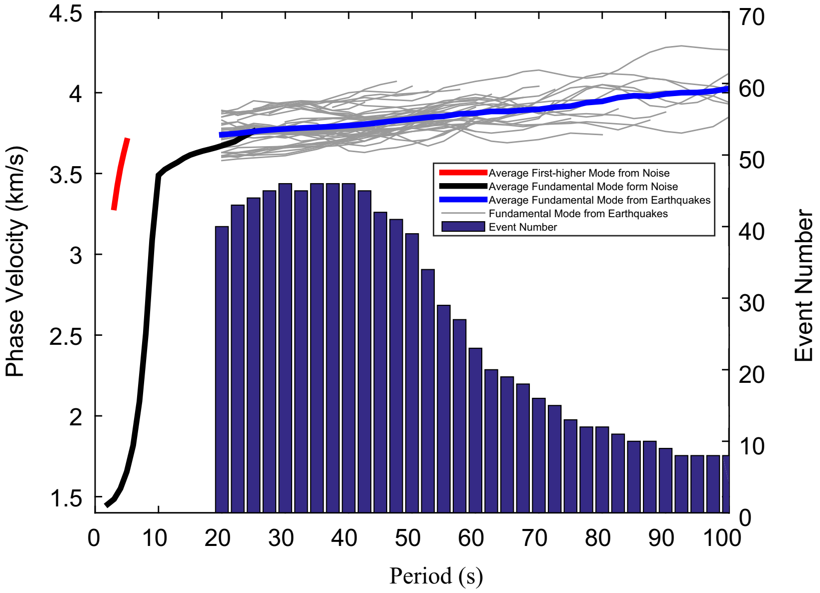

Figure 6. Rayleigh-wave phase-velocity dispersion curves and the associated number of teleseismic events. The grey lines are the fundamental-mode phase velocity measured from all selected teleseismic events. The blue histogram gives the number of teleseismic events used at different periods. The blue line is the average fundamental-mode phase-velocity dispersion curve from all teleseismic events (period band 20–100 s). The red line is the average first-higher-mode phase-velocity dispersion curve from ambient noise (period band 3–7 s), and the black line is the average fundamental-mode phase-velocity dispersion curve from ambient noise (period band 2–25 s) from Yao *et al.* (2011).

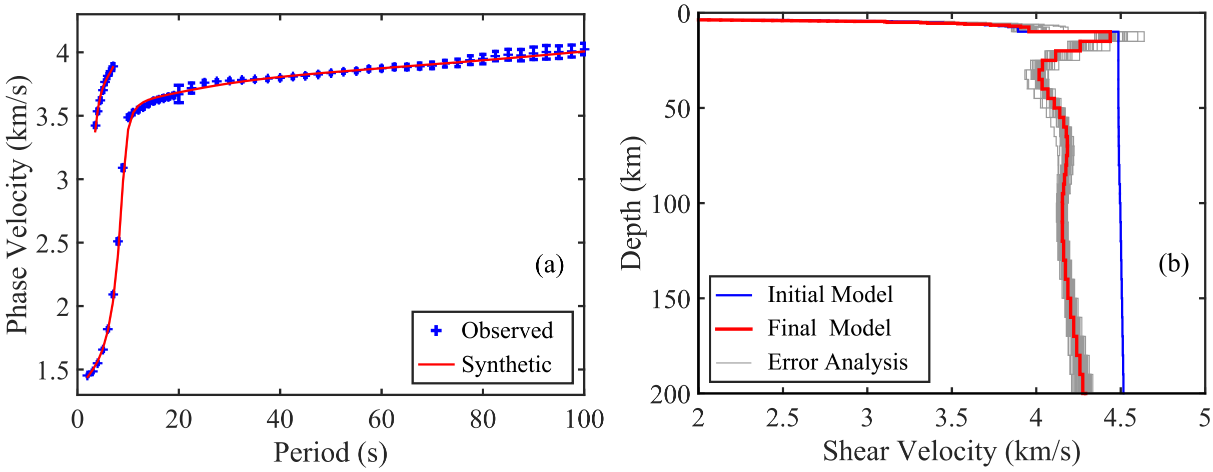

Figure 7. Average Rayleigh-wave dispersion and the shear velocity structure inversion of the DG region. (a) The blue cross and the error bar give the observed average Rayleigh-wave phase-velocity dispersion and the standard error of the mean, respectively (Fig. 6). The red line is the synthetic dispersion calculated from the final Vs model [the red line in panel (b) & Table 1]. (b) The blue line is the initial Vs model with its crustal part from Yao *et al.* (2011), and the upper-mantle part from Kennett *et al.* (1995) and Montagner & Kennett (1996). The red line is the final Vs model. The grey lines are the 100 models obtained using the dispersion data with random noise added.

inversion. We repeat 100 times of this random noise test and show all the inversion results in Fig. 7(b). The standard errors of Vs from these models at different depths are mostly smaller than 0.1 km s^{-1}.

The average shear velocity of the upper-mantle structure is 4.18 km s^{-1} between the Moho and 200-km depth. This upper-mantle structure can be simply divided into three main parts: a high-velocity LID, the pronounced part of an LVZ (pronounced LVZ) and the weak part of the LVZ (weak LVZ) (Fig. 9). The LID exits just beneath the Moho in the depth range about 10–15 km. The maximum Vs of the LID is about 4.37 km s^{-1}, which is lower than that of other older regions of the Pacific Ocean from previous studies (Nishimura & Forsyth 1989; Harmon *et al.* 2007; Weeraratne *et al.* 2007). If we define the pronounced LVZ as the contiguous zone just beneath the LID with its Vs less than 4.15 km s^{-1}, then the depth range of the pronounced LVZ is 15–60 km below the sea level. The minimum Vs of the pronounced LVZ is 4.03 km s^{-1} at a depth range of 30–35 km. Compared with some other LVZs beneath older Pacific regions, the minimum Vs of the pronounced LVZ beneath our study region is slightly higher (less than 0.1 km s^{-1}), the thickness is thinner, and the depth distribution is shallower

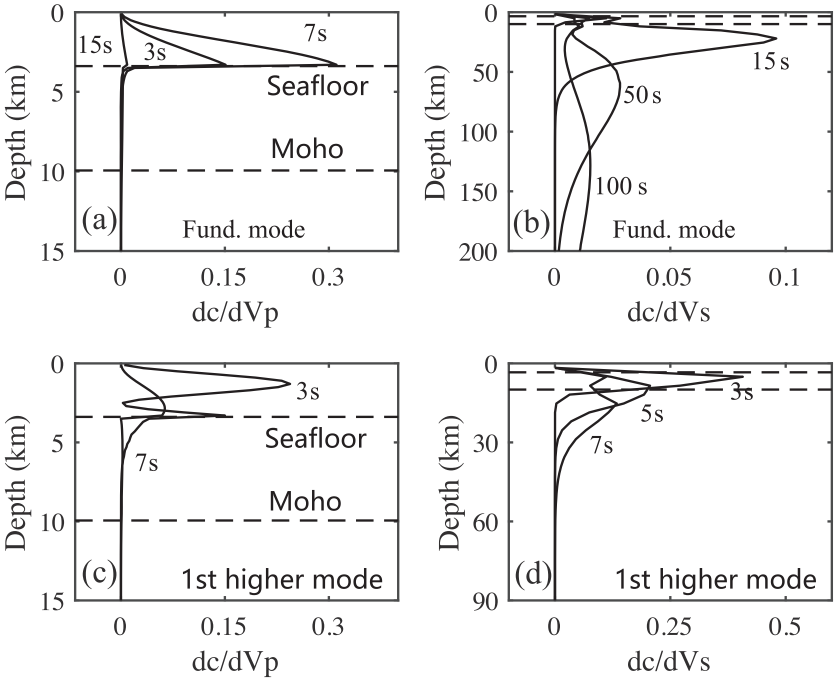

Figure 8. Rayleigh-wave phase-velocity (c) sensitivity kernels to Vp (a) and Vs (b) for the fundamental mode and Vp (c) and Vs (d) for the first-higher mode at selected periods. These sensitivity kernels are calculated based on our final model in Fig. 7(b). The black dashed lines at the 3.3-km depth and 9.9-km depth represent the seafloor and the Moho interface from Yao *et al.* (2011).

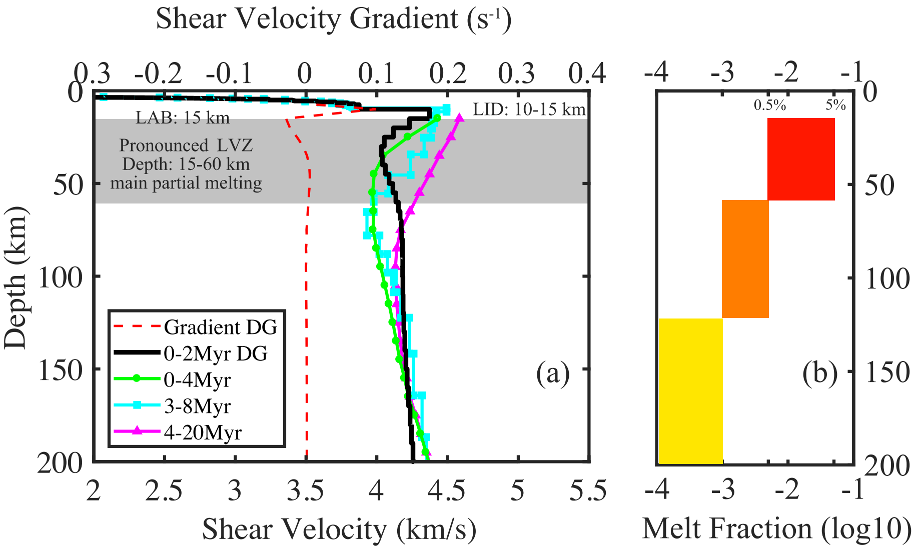

Figure 9. The average shear velocity model and melt fraction of the upper mantle beneath the DG region. (a) Average Vs model. The black line is the final Vs model of the DG region after inversion (see Fig. 7b and Table 1). The green and magenta lines are the Vs models from Nishimura & Forsyth (1989). The cyan line is the Vs model from Weeraratne *et al.* (2007) & Harmon *et al.* (2007). The red dashed line is the gradient of our shear velocity model. (b) Our estimation of the melt fraction of different parts in our model based on the studies of Hirschmann *et al.* (2009) and Hirschmann (2010).

Table 1. The upper-mantle shear velocity structure in the DG region after inversion (see Figs 7a and 9). The depth is the top depth of each layer, and the depth of the Moho interface is 9.94 km.

Depth (km)	9.94	15	20	25	30	35	40	45	50	55
Vs (km s^{-1})	4.37	4.23	4.12	4.05	4.03	4.04	4.06	4.09	4.11	4.13
Depth (km)	60	65	70	75	80	85	90	95	100	110
Vs (km s^{-1})	4.15	4.16	4.17	4.18	4.18	4.18	4.18	4.18	4.18	4.19
Depth (km)	120	130	140	150	160	170	180	190	200	
Vs (km s^{-1})	4.19	4.20	4.21	4.21	4.22	4.24	4.25	4.26	4.27	

(Fig. 9). At the larger depth of our model, there is the weak LVZ at 60–200 km below the sea level with an average Vs of 4.20 km s^{-1}, about 0.3 km s^{-1} lower than the global model (Fig. 7b). As shown in Fig. 9, there is no remarkable difference (< 0.1 km s^{-1}) between the Vs below 120-km depth among four models of different lithospheric ages.

5 DISCUSSION

5.1 Dispersion analysis

The teleseismic surface wave dispersion analysis method developed in this study has some obvious advantages and disadvantages. At the beginning of this study, we attempted to use the traditional TS analysis method (e.g. Yao *et al.* 2006). But we found that the dispersion curves from TS analysis are difficult to measure and unstable for individual station pairs, especially at the periods longer than 60 s (Fig. 5c). This may be attributed to the low signal-to-noise ratio (SNR) of OBSs data at longer periods. Considering the SNR and the distribution of these OBSs in Fig. 1, we therefore developed this array-based dispersion analysis method to obtain more stable average phase velocities from multiple stations simultaneously, instead of using the traditional TS analysis method or the frequency–time analysis method (FTAN; e.g. Levshin & Ritzwoller 2001; Lin *et al.* 2007). Furthermore, the dispersion curve tracing of our method is based on a 3-D amplitude matrix instead of the 2-D image of TS or FTAN in order to use the continuity constraint of group velocity and phase velocity dispersion (Fig. 5a). Based on the combined dispersion characteristics, it is also easier to find the fundamental mode signals for dispersion tracing.

The array-based multidimensional imaging analysis method presented in this paper is more suited to obtain stable dispersion for the inversion of a 1-D Vs structure beneath a linear station array. But if there is a planar array with good station distribution and high SNR data, the two-plane-wave earthquake tomography method (e.g. Yang & Ritzwoller 2008) and the Helmholtz surface wave tomography method (e.g. Lin & Ritzwoller 2011) are recommended for the inversion of 3-D Vs structures. The phase velocity measurements from teleseismic events and ambient noise are slightly different (Fig. 6, period range: 20–25 s). Yao *et al.* (2006) mentioned several factors could contribute to this discrepancy. In this study, we think the main factor is off-great-circle propagation. In addition, the scattering effects, finite frequency effects, and seismic anisotropy are all ignored in this study because of the limited resolution of data.

5.2 LAB and the test of the conductive cooling model

We estimated the thickness of the oceanic lithosphere beneath our study region (Fig. 9 and Table 1) and found that it is fairly consistent with the conductive cooling model of oceanic lithosphere (Harmon *et al.* 2009). The sharp decrease from LID to LVZ is generally termed the G-discontinuity (Revenaugh & Jordan 1991). The definition of lithosphere and asthenosphere in tectonic/geodynamic layering is based on its mechanical strength, so the lithosphere–asthenosphere boundary (LAB) is a mechanical interface (Kawakatsu & Utada 2017). Although we cannot tell whether an interface or a discontinuity is a LAB simply from seismological observation alone, some recent seismological studies considered the G-discontinuity as the LAB (Kawakatsu & Utada 2017). In this study, we assumed the LAB as the layer corresponding to the maximum of the negative velocity gradient (Weeraratne *et al.* 2003). So the averaged thickness of lithosphere beneath this study region can be estimated as 15 ± 2.5 km (Fig. 9). According to the thermal half-space cooling model of the oceanic lithosphere (eq. 4.126 in Turcotte & Schubert 2002), we calculated the thickness of the lithosphere at the age of 1–2 Myr to be 13–18 km. On the other hand, based on the station distribution in Fig. 1 and the half-spreading rate of ∼70 mm yr^{-1} in this mid-oceanic ridge region (Pickle *et al.* 2009), we estimated the ocean-floor age of this study region to be 0–2 Myr. These numbers are consistent with the predictions of the conductive cooling model. Furthermore, because of the younger age, the temperature of lithosphere may be higher. Hence the Vs of the LID in this region is also lower (∼0.1–0.2 km s^{-1}) than in some older regions (∼3–20 Myr) of the Pacific Ocean (Fig. 9). In addition, because the ray paths are approximately subparallel to the spreading direction, the measured phase velocity is likely along the fast direction of olivine spreading fabric in the upper mantle. Thus, the true azimuthally averaged isotropic SV velocity (Vsv) in the upper mantle is probably even slower than measured in this study.

5.3 Interpretation of the LVZ

The MOR is the place where the new oceanic lithosphere is created from the uprising magma, which is likely supplied by a partial melting zone in the upper mantle beneath the MOR. Such a partial melting zone generally corresponds to the LVZ observed in seismological studies (Hammond & Humphreys 2000). Above the dry solidus line, there should be a large amount of partial melting with or without volatiles (H_2O and CO_2), which may correspond to a pronounced LVZ. Below the dry solidus line, volatiles play more important roles in generating partial melting. Because even small amounts of volatiles could significantly reduce the solidus temperature, partial melting may occur at larger depth (Kawakatsu & Utada 2017), likely corresponding to a weak LVZ observed in this and other studies.

Our results show that the shear velocity of the upper mantle beneath the DG region is about 5–10 per cent lower than the global average. Although the amount of melt is not well constrained by using the Vs model alone, we can still provide a preliminary estimate of the melt fraction (Hirschmann 2010) in the upper mantle (15–200 km). We consider our study region as a typical MOR basalt source region, with 100 ppm H_2O and 60 ppm CO_2 (Hirschmann 2010). As mentioned before, There is no remarkable difference among different-age models below 120 km (Fig. 9). The inferred melt fraction of this deepest part is less than 0.1 per cent. The actual melting may be a complex combination of the formation of carbonated silicate melts and dehydration melting (Dasgupta *et al.* 2007). The depth range of the middle part is 60–120 km. The melt fraction of this part is estimated to be ∼0.1–0.5 per cent, likely corresponding to dehydration melting. The depth range of the shallowest part is 15–60 km with a pronounced LVZ. The temperature of the MOR geotherm of this depth range could be above the dry solidus line (Fig. 10a), so there would be a large amount of partial melting even without volatiles. The melt fraction may be from ∼0.5 per cent to ∼5 per cent (Forsyth *et al.* 1998).

5.4 Comparison with other regions

Fig. 9 shows a comparison of the Vs model in this study and some other regions with older oceanic crust. The main difference between them is at ∼15–120-km depth. At the shallow depth (∼15–30 km), the Vs of our model is lower than the rest. Then it starts to increase

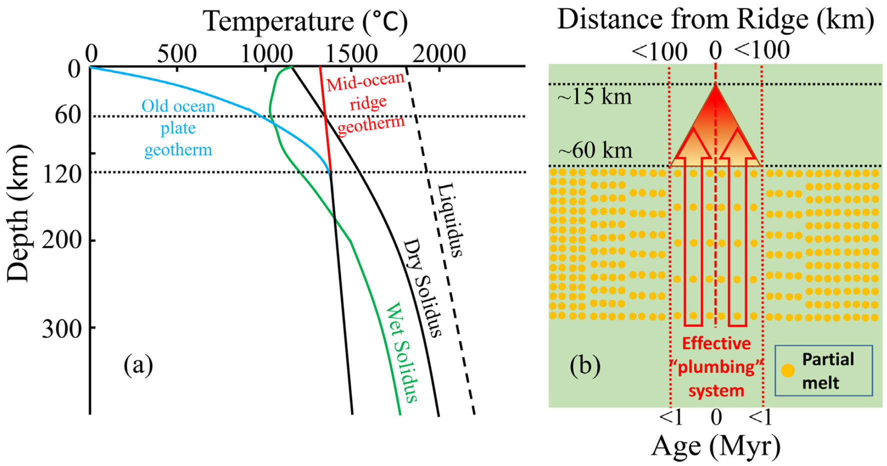

Figure 10. Schematic diagrams of the two possible mechanisms mentioned in Section 5.4. (a) A schematic plot of the solidus and geotherms. The red line is the geotherm of a very young mid-ocean ridge (e.g. <1 Myr in this study). The blue line is the geotherm of old ocean plates. The green line is the wet solidus. The black line is the dry solidus. The black dashed line is the liquidus. (b) A schematic plot of the effective 'plumbing' system for melt upwelling beneath the EPR ridge (Harmon *et al.* 2009). The yellow dots denote partial melts. The red triangle shows the main partial-melting (∼0.5 per cent to ∼5 per cent) zone, which is also the pronounced LVZ beneath the centre of the ridge (Fig. 9). The red arrows are the channels of the potential effective 'plumbing' system. The melt at large depths beneath the very young region (e.g. <1 Myr in this study) could quickly upwell to the shallow pronounced LVZ. However, the melt beneath older regions (e.g. several Myr) could not effectively upwell to the upper zone.

and is higher than the rest at ∼30–120-km depth. These differences mainly come from the plate ages. Four detailed factors may contribute to these differences. (1) The geotherms beneath oceanic regions with different ages are different (Fig. 10a). We estimate that only the geotherm of the very young region (e.g. <1 Myr) could cross the dry solidus. So, there would be a large amount of partial melting at the shallow (∼30-km) depth beneath this very young oceanic region (Fig. 10b). At the ∼60-km-depth cross-point (Fig. 10a), the Vs starts to decrease along the direction from deep to shallow (Fig. 9). Because we average different-age oceanic regions into a 1-D structure, our Vs model (0–2 Myr) is more similar to the structure of this very young region, rather than other Vs models in Fig. 9 (e.g. 0–4, 3–8 and 4–20 Myr). In addition, the Vs at 30 km of our model and the Vs at 70 km of 0–4 Myr and 3–8 Myr models are all about 4 km s^{-1}. However, we infer that the melt fraction of our model at 30 km is much larger than that at 70 km of the other two older models (Fig. 9). (2) As for the reason why the Vs of our model is higher than other models of older regions at ∼30–120-km depth, it may be because that there is an effective 'plumbing' system beneath the EPR ridge (Harmon *et al.* 2009). We speculate that this effective 'plumbing' system only exists around the central ridge region (e.g. <100 km or <1 Myr, see Fig. 10b). The melt at larger depth beneath the very young region (<1 Myr in this study) could quickly upwell to the shallow pronounced LVZ. Such melt removal beneath this young region could cause an increase of Vs at ∼30–120-km depth as shown in our model. However, the melt beneath other older regions (e.g. several Myrs) could not effectively upwell to the upper zone. So, the Vs of these older regions is likely lower. (3) The resolution of the results (0–4 and 4–20 Myr) of Nishinura & Forsyth (1989) is limited by the data quality and availability used for the inversion of the entire Pacific Ocean. (4) Most of the measurements of Nishinura & Forsyth (1989) are on the east side of the EPR with younger plate ages. But our measurements are on the west side and central part of the EPR (Fig. 1). The Vs structure beneath the EPR region may be asymmetric, as found in previous studies (Dunn & Forsyth 2003; Harmon *et al.* 2009).

6 CONCLUSIONS

Based on the array-based multidimensional imaging analysis method developed for teleseismic surface wave dispersion analysis, we obtained an average 1-D upper mantle Vs model beneath the DG transform fault region on the equatorial EPR. Our final model shows a thin (∼5-km thickness) high-velocity LID in the uppermost mantle with the maximum Vs at 4.37 km s^{-1} beneath the Moho, and a pronounced LVZ between 15-km and 60-km depth in the uppermost mantle with Vs about 4.03–4.23 km s^{-1} which is about 10 per cent lower than the global average and indicates about 0.5–5 per cent melt fraction. Between 60 and 200 km, a weak LVZ exists with Vs about 4.15–4.27 km s^{-1}, which is about 5 per cent lower than the global average with about 0.1 per cent or even lower melt fraction. We inferred that the averaged LAB beneath this study region is about 15 km, which is consistent with the conductive cooling model. The shallower and thinner characteristics of the pronounced LVZ beneath this region may imply that partial melting occurs mainly in the shallow upper mantle (∼15–60-km depth) in this young oceanic region, probably with an effective 'plumbing' system for melt upwelling.

ACKNOWLEDGEMENTS

We thank all the scientists and crew for their work of the seismic experiment at the Quebrada/Discovery/Gofar region on the East Pacific Rise, which is conducted by the Woods Hole Oceanographic Institution (WHOI). Seismic data analysed in this study are archived at IRIS Data Management Center (http://ds.iris.edu/mda/ZD?timewindow=2007–2009, last accessed June 2018). Some figures are plotted by using the Generic Mapping Tools (Wessel & Smith 1998), Version 5.1.2 (http://gmt.soest.hawaii.edu/). This work is supported by the National Natural Science Foundation of China (grant numbers 41574034 and 41222028). We thank two anonymous reviewers, the associate editor, and editor Carl Tape for their constructive comments, which help us improve the manuscript.

REFERENCE

Ball, J.S., Sheehan, A.F., Stachnik, J.C., Lin, F.C., Yeck, W.L. & Collins, J.A., 2016. Lithospheric shear velocity structure of South Island, New Zealand, from amphibious Rayleigh wave tomography, *J. geophys. Res.,* **121**(5), 3686–3702.

Beaulieu, S.E. & Szafranski, K., 2019. *InterRidge Global Database of Active Submarine Hydrothermal Vent Fields,* Version 3.4, World Wide Web electronic publication available, Accessed 2019 July 24, http://vents-data.interridge.org

Brocher, T.M., 2005. Empirical relations between elastic wavespeeds and density in the Earth's crust, *Bull. seism. Soc. Am.,* **95**(6), 2081–2092.

Dasgupta, R., Hirschmann, M.M. & Smith, N.D., 2007. Water follows carbon: CO2 incites deep silicate melting and dehydration beneath mid-ocean ridges, *Geology,* **35**(2), 135–138.

Dunn, R.A. & Forsyth, D.W., 2003. Imaging the transition between the region of mantle melt generation and the crustal magma chamber beneath the southern East Pacific Rise with short-period Love waves, *J. geophys. Res.,* **108**(B7), 2352.

Evans, R.L., Hirth, G., Baba, K., Forsyth, D., Chave, A. & Mackie, R., 2005. Geophysical evidence from the MELT area for compositional controls on oceanic plates, *Nature,* **437**(7056), 249–252.

Forsyth, D.W., Harmon, N., Scheirer, D.S. & Duncan, R.A., 2006. Distribution of recent volcanism and the morphology of seamounts and ridges in the GLIMPSE study area: implications for the lithospheric cracking hypothesis for the origin of intraplate, non–hot spot volcanic chains, *J. geophys. Res.,* **111**(B11407), doi:10.1029/2005JB004071.

Forsyth, D.W., Webb, S.C., Dorman, L.M. & Shen, Y., 1998. Phase velocities of Rayleigh waves in the MELT experiment on the East Pacific Rise, *Science,* **280**(5367), 1235–1238.

Froment, B., McGuire, J.J., van der Hilst, R.D., Gouédard, P., Roland, E.C., Zhang, H. & Collins, J.A., 2014. Imaging along-strike variations in mechanical properties of the Gofar transform fault, East Pacific Rise, *J. geophys. Res.,* **119**(9), 7175–7194.

Gu, Y.J., 2005. Upper mantle structure beneath the eastern Pacific Ocean ridges, *J. geophys. Res.,* **110**(B06305).

Géli, L., Piau, J.-M., Dziak, R., Maury, V., Fitzenz, D., Coutellier, Q. & Henry, P., 2014. Seismic precursors linked to highly compressible fluids at oceanic transform faults, *Nat. Geosci.,* **7,** 757–761.

Hammond, W.C. & Humphreys, E.D., 2000. Upper mantle seismic wave velocity: effects of realistic partial melt geometries, *J. geophys. Res.,* **105**(B5), 10 975–10 986.

Harmon, N., Forsyth, D. & Webb, S., 2007. Using ambient seismic noise to determine short-period phase velocities and shallow shear velocities in the young oceanic lithosphere, *Bull. seism. Soc. Am.,* **97**(6), 2009–2023.

Harmon, N., Forsyth, D. & Weeraratne, D., 2009. Thickening of young Pacific lithosphere from high-resolution Rayleigh wave tomography: A test of the conductive cooling model, *Earth planet. Sci. Lett.,* **278**(1), 96–106.

Herrmann, R.B., 2013. Computer programs in seismology: an evolving tool for instruction and research, *Seismol. Res. Lett.,* **84**(6), 1081–1088.

Hirschmann, M.M., 2010. Partial melt in the oceanic low velocity zone, *Phys. Earth planet. Inter.,* **179**(1-2), 60–71.

Hirschmann, M.M., Tenner, T., Aubaud, C. & Withers, A.C., 2009. Dehydration melting of nominally anhydrous mantle: the primacy of partitioning, *Phys. Earth planet. Inter.,* **176**(1-2), 54–68.

Kawakatsu, H. & Utada, H., 2017. Seismic and electrical signatures of the lithosphere–asthenosphere system of the normal oceanic mantle, *Annu. Rev. Earth Planet. Sci.,* **45,** 139–167.

Kennett, B.L.N., Engdahl, E.R. & Buland, R., 1995. Constraints on seismic velocities in the earth from travel-times, *Geophys. J. Int.,* **122**(1), 108–124.

Langmuir, C.H. & Forsyth, D.W., 2007. Mantle melting beneath mid-ocean ridges, *Oceanography,* **20**(1), 78–89.

Levshin, A.L. & Ritzwoller, M.H., 2001. Automated detection, extraction, and measurement of regional surface waves, *Pure appl. Geophys.,* **158,** 1531–1545.

Lin, F.-C. & Ritzwoller, M.H., 2011. Helmholtz surface wave tomography for isotropic and azimuthally anisotropic structure, *Geophys. J. Int.,* **186**(3), 1104–1120.

Lin, F.-C., Ritzwoller, M.H., Townend, J., Bannister, S. & Savage, M.K., 2007. Ambient noise Rayleigh wave tomography of New Zealand, *Geophys. J. Int.,* **170**(2), 649–666.

Lin, P.Y.P., Gaherty, J.B., Jin, G., Collins, J.A., Lizarralde, D., Evans, R.L. & Hirth, G., 2016. High-resolution seismic constraints on flow dynamics in the oceanic asthenosphere, *Nature,* **535**(7613), 538–541.

McGuire, J.J., 2008. Seismic cycles and earthquake predictability on East Pacific Rise transform faults, *Bull. seism. Soc. Am.,* **98**(3), 1067–1084.

McGuire, J.J., Boettcher, M.S. & Jordan, T.H., 2005. Foreshock sequences and short-term earthquake predictability on East Pacific Rise transform faults, *Nature,* **434**(7032), 457–461.

McGuire, J.J., Collins, J.A., Gouédard, P., Roland, E., Lizarralde, D., Boettcher, M.S., Behn, M.D. & van der Hilst, R.D., 2012. Variations in earthquake rupture properties along the Gofar transform fault, East Pacific Rise, *Nat. Geosci.,* **5**(5), 336–341.

Montagner, J.P. & Kennett, B.L.N., 1996. How to reconcile body-wave and normal-mode reference earth models, *Geophys. J. Int.,* **125**(1), 229–248.

Nishimura, C.E. & Forsyth, D.W., 1989. The anisotropic structure of the upper mantle in the Pacific, *Geophys. J. Int.,* **96**(2), 203–229.

Pickle, R.C., Forsyth, D.W., Harmon, N., Nagle, A.N. & Saal, A., 2009. Thermo-mechanical control of axial topography of intra-transform spreading centers, *Earth planet. Sci. Lett.,* **284**(3), 343–351.

Revenaugh, J. & Jordan, T.H., 1991. Mantle layering from ScS reverberations: 1. Waveform inversion of zeroth-order reverberations, *J. geophys. Res.,* **96**(B12), 19 749–19 762.

Roland, E., Lizarralde, D., McGuire, J.J. & Collins, J.A., 2012. Seismic velocity constraints on the material properties that control earthquake behavior at the Quebrada-Discovery-Gofar transform faults, East Pacific Rise, *J. geophys. Res.,* **117**(B11102), doi:10.1029/2012JB009422.

Takeo, A., Kawakatsu, H., Isse, T., Nishida, K., Shiobara, H., Sugioka, H., Ito, A. & Utada, H., 2018. In situ characterization of the lithosphere-asthenosphere system beneath NW Pacific Ocean via broadband dispersion survey with two OBS arrays, *Geochem. Geophys. Geosyst.,* **19**(9), 3529–3539.

Takeo, A., Kawakatsu, H., Isse, T., Nishida, K., Suetsugu, D., Shiobara, H., Sugioka, H. & Ito, A., 2016. Intensity of seismic azimuthal anisotropy in the oceanic lithosphere and asthenosphere from broadband surface-wave analysis of OBS array records at 60 Ma seafloor, *J. geophys. Res.,* **121,** 1927–1947.

Takeo, A., Nishida, K., Isse, T., Kawakatsu, H., Shiobara, H., Sugioka, H. & Kanazawa, T., 2013. Radially anisotropic structure beneath the Shikoku Basin from broadband surface wave analysis of ocean bottom seismometer records, *J. geophys. Res.,* **118**(6), 2878–2892.

Turcotte, D.L. & Schubert, G., 2002. *Geodynamics,* 2nd edn, Cambridge Univ. Press, p. 287.

Webb, S.C. & Forsyth, D.W., 1998. Structure of the upper mantle under the EPR from waveform inversion of regional events, *Science,* **280**(5367), 1227–1229.

Weeraratne, D.S., Forsyth, D.W., Fischer, K.M. & Nyblade, A.A., 2003. Evidence for an upper mantle plume beneath the Tanzanian craton from Rayleigh wave tomography, *J. geophys. Res.,* **108**(B9), 2427.

Weeraratne, D.S., Forsyth, D.W., Yang, Y. & Webb, S.C., 2007. Rayleigh wave tomography beneath intraplate volcanic ridges in the South Pacific, *J. geophys. Res.,* **112**(B06303), doi:10.1029/2006JB004403.

Wei, S.S., Zha, Y., Shen, W., Wiens, D.A., Conder, J.A. & Webb, S.C., 2016. Upper mantle structure of the Tonga-Lau-Fiji region from Rayleigh wave tomography, *Geochem. Geophys. Geosyst.,* **17**(11), 4705–4724.

Wessel, P. & Smith, W.H., 1998. New, improved version of Generic Mapping Tools released, *EOS, Trans. Am. geophys. Un.,* **79**(47), 579–579.

Wolfson-Schwehr, M., Boettcher, M.S., McGuire, J.J. & Collins, J.A., 2014. The relationship between seismicity and fault structure on the Discovery transform fault, East Pacific Rise, *Geochem. Geophys. Geosyst.,* **15**(9), 3698–3712.

Yang, Y. & Ritzwoller, M.H., 2008. Teleseismic surface wave tomography in the western U.S. using the Transportable Array component of USArray, *Geophys. Res. Lett.,* **35**(L04308), doi:10.1029/2007GL032278.

Yao, H.J., Gouedard, P., Collins, J.A., McGuire, J.J. & van der Hilst, R.D., 2011. Structure of young East Pacific Rise lithosphere from ambient noise correlation analysis of fundamental- and higher-mode Scholte-Rayleigh waves, *C.R. Geosci.,* **343**(8), 571–583.

Yao, H.J., van der Hilst, R.D. & de Hoop, M.V., 2006. Surface-wave array tomography in SE Tibet from ambient seismic noise and two-station analysis—I. Phase velocity maps, *Geophys. J. Int.,* **166**(2), 732–744.

SUPPORTING INFORMATION

Supplementary data are available at *GJI* online.

1. Additional material on phase velocity data.
2. Additional test with 2–60 s dispersion data.
3. Additional tests with different damping values.

Figure S1. The black parts of dispersion curves are the same as the grey lines in Fig. 6 of the main text. All the black parts are used to calculate the average dispersion curve and error estimation. The grey parts in this figure are the removed parts.

Figure S2. Final Vs models of the inversion from 2 to 100 s data (red) and 2 to 60 s data (blue). The red line is the same as that in Fig. 7(b).

Figure S3. The comparison between the results of damping = 1 and damping = 2. The misfits of these two damping values are almost the same [see panel (a) and Table S1]. The final Vs models are slightly different. The result of damping = 2 has only one minimum of the Vs model below 15-km depth, which means it has only one LVZ in the upper mantle.

Table S1. The dispersion misfits of the 1-D shear velocity inversion with different damping values. These L1-norm misfits are averaged by the number of dispersion data points (Fig. 7a). The final damping value is set as 2 in this study (Figs 7b and 9 of the main text, and Fig. S2).

Please note: Oxford University Press is not responsible for the content or functionality of any supporting materials supplied by the authors. Any queries (other than missing material) should be directed to the corresponding author for the paper.